Flame Transfer Functions and Dynamics of a Closely Confined Premixed Bluff Body Stabilized Flame With Swirl

Håkon T. Nygård[1]
Department of Energy and Process Engineering,
Norwegian University of
Science and Technology,
Trondheim 7491, Norway
e-mail: hakon.t.nygard@ntnu.no

Nicholas A. Worth
Department of Energy and Process Engineering,
Norwegian University of
Science and Technology,
Trondheim 7491, Norway

The flame transfer function (FTF) and flame dynamics of a highly swirled, closely confined, premixed flame is studied over a wide range of equivalence ratios and bulk velocities at a fixed perturbation level at the dump plane. The operating conditions are varied to examine the ratio of flame height to velocity in scaling the FTF. The enclosure geometry is kept constant, resulting in strong flame-wall interactions for some operating conditions due to varying flame height. The resulting effect on the FTF due to changes in the "effective flame confinement" can therefore be studied. For sufficiently high equivalence ratio, and the resulting sufficiently small effective confinement, modulations of the FTF are observed due to interference of the perturbations created at the swirler and at the dump plane. The small length scales and high velocities result in modulations centered at high frequencies and spanning a wide range of frequencies compared to previous studies of similar phenomena. A critical point was reached for increasing effective confinement, where the modulations are suppressed. This is linked to a temporal shift in the heat release rate where the flame impinges on the combustion chamber walls. The shift reduced the expected level of interference, demonstrating effective confinement is important for the FTF response. Additionally, a distributed time lag (DTL) model with two time lags is successfully applied to the FTFs, providing a simple method to capture the two dominant time scales in the problem, recreate the FTF, and examine the effect of effective confinement. [DOI: 10.1115/1.4049513]

Introduction

The occurrence of thermoacoustic instabilities is an issue which may restrict fuel and operational flexibility in gas turbine engines, hindering the development of low emission systems. Such instabilities arise due to the unsteady interaction and growth of heat release rate and pressure oscillations inside the combustor, which can reach damaging levels [1], and therefore must be eliminated during design.

A common framework to predict such instabilities during the design phase relies on accurate knowledge of the magnitude and delay of a flame's heat release rate oscillations, in response to reference input oscillations over a range of frequencies and amplitudes. Such response functions are denoted as flame transfer functions (FTF) which are valid for low and moderate oscillation amplitudes, where the response is assumed to be linear, or flame defining functions if these also capture high amplitude and specifically the nonlinear response of the flame. When known, these functions can be used in low-order network [2–4] or more involved Helmholtz [5] solvers to predict the system stability. The potential utility of this approach, in reducing the significant complexity associated with the reacting flow to a simple response function, has resulted in considerable effort in understanding the behavior, scaling, and generality of such functions [6–11].

In particular, a number of recent studies have focused on understanding the presence of multiple time scales in the response, due to vorticity oscillations generated both at the injector lip and further upstream from the swirler geometry [7–9], or from nonuniform mixtures and therefore equivalence ratio oscillations [6]. In this study, the response of a closely confined premixed swirling flame will be investigated, and therefore in terms of multiple time scales, it is interesting to review previous studies which have examined interference effects from an upstream swirler.

Previous studies have focused on the effect of the location of an axial swirler [7,12,13], the difference between axial and tangential inlet swirler [10], the influence of swirl number [9], or the geometry of the injector [14]. A common feature of all of these studies is the effective *interference* which can be introduced under certain conditions, resulting from the interaction between velocity oscillations generated at the combustor inlet and the upstream convective vorticity oscillations generated at the swirler. The interference can result in modulations in the gain and phase of the transfer function, with the variation in gain manifesting as a characteristic minima or *dip*. Some of these physical interference phenomena were described in a series of papers by Palies et al., demonstrating convective oscillations modulate the swirl number, which can interfere either constructively or destructively with the vorticity oscillations generated at the inlet [8,15]. Gatti et al. [14] showed two vortex shedding locations are required to generate interference by using an upstream swirler and a bluff body at the combustion chamber inlet. Recently, Æsøy et al. [16] made this more explicit, by showing the interference could be generated by replacing the swirler with round cylinders (grub screws). The presence of multiple sources of vortex shedding can be modeled through the inclusion of multiple time scales, and thus multiple Strouhal numbers. Kim and Santavicca [6] show that a combination of Strouhal number scalings is most effective for collapsing the flame response in the presence of multiple time delays. This use of multiple scaling parameters is similarly taken by Sattelmayer [17] with multiple distributed time lags (DTLs). This approach has been used successfully, for example, by Schuermans et al. [18] and Schimek et al. [11] who use two DTLs to model both equivalence ratio and acoustic oscillations.

Another geometric parameter of relevance in this study is the confinement ratio of the combustor. Several studies have shown that changing the confinement of the flame results in flame shape changes, which in turn affects the FTF [19–21]. More recently, De

[1]Corresponding author.

Manuscript received October 9, 2020; final manuscript received October 14, 2020; published online February 26, 2021. Editor: Jerzy T. Sawicki.

Rosa et al. [22] studied the effect of changing confinement in a configuration featuring multiple time delays, finding that confinement can have significant influence in modulating the transfer function response. The frequency scaling could be somewhat captured by basing the time delay on the flame height, allowing a scaling of the minima. However, a significant change was also observed in the FTF gain at low frequencies, which was linked to the increasingly noncompact behavior of the more closely confined and therefore elongated flame.

The aim of this study is to characterize the response of a perfectly premixed swirling bluff body stabilized flame, confined within a square enclosure. The injector geometry under investigation is almost identical to the one used in a number of previous studies of self-excited thermoacoustic instabilities in annular enclosures [23,24]. Therefore, it is of interest to define the response function for this injector to permit stability predictions to be made for this annular configuration, and this is likely useful in terms of modeling practically relevant annular systems. Additionally, the characteristic geometric features of this particular configuration result in a number of interesting features in the response, as a result of both multiple response time delays, the relatively close confinement, and asymmetry effects. Therefore, a further aim of this study is to examine the response with reference to these influences, and assess the performance of a multiple delay model in accurately capturing these. In particular, the influence of the relative confinement on the dip behavior typically associated with swirling flames will be highlighted.

Experimental Setup and Methods

The setup used for the experiments is shown in Fig. 1. The reactants, air and ethylene, were mixed in the supply lines and the mixture is considered perfectly premixed when injected into the plenum. After entering the plenum, the reactants pass through a honeycomb flow straightener. Above the flow straightener, two horn drivers (Adastra HD60) are mounted diametrically opposite each other. These are driven in phase to create flow perturbations

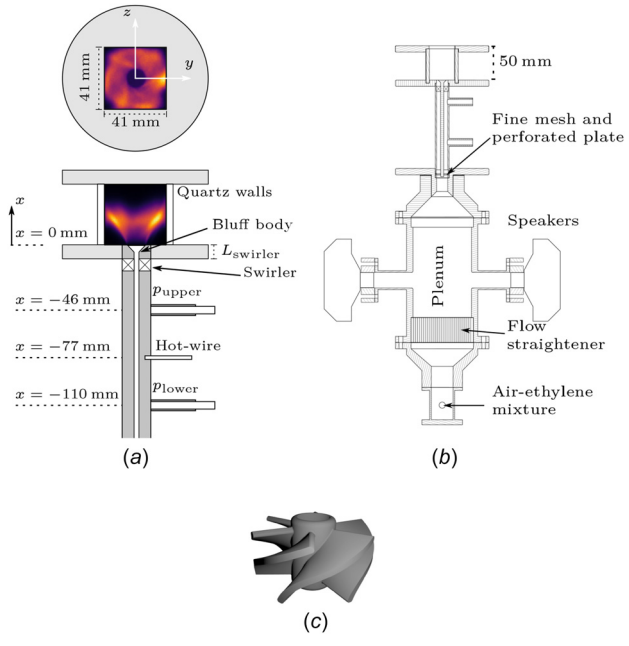

Fig. 1 Experimental setup with key dimensions and equipment with top view in (*a*), the full setup in (*b*), and a 3D model of the swirler in (*c*). Cameras were aligned with the *z*-axis, with the top view achieved by a 45 deg mirror mounted directly above the flame. The photomultiplier tube is aligned with the *y*-axis: (*a*) Close side and top view, (*b*) full setup view, and (*c*) swirler.

that result in velocity fluctuations at the burner dump plane. The flow passes through a conic contraction before entering the injection tube.

The injection tube geometry is exactly the same as that used in previous investigations of combustion instabilities in annular chambers [25] (and almost identical to Refs. [23] and [24]), shown in detail in Fig. 1(*a*). The injector tube has a length of 145mm, and a bluff body with a swirler is mounted in the center. The bluff body has a final diameter $d_{bb} = 13$mm and half angle 45 deg and is mounted on a rod of diameter 5mm. The swirler, shown in detail in Fig. 1(*c*), produces an anticlockwise swirl when observed from downstream, and the trailing edge of the swirler is oriented at an angle $\alpha = 60$ deg. The axial distance from the trailing edge of the swirler vanes to the dump plane is $L_{swirler} = 10$mm. Based on geometric considerations, the swirl number will be $S_{geometry} = 1.22$ right after the swirler [23], but is reduced at the exit due to the contraction. The swirl number has been measured to be approximately $S_{exp} = 0.65$ in an unconfined configuration 10mm downstream of the injector exit.

At the dump plane, the injector exit has a diameter $d_{exit} = 19$mm, giving a blockage ratio of 47%. The combustion chamber side walls are made of quartz for optical access and form a square enclosure of dimensions $41 \times 41 \times 50$mm. The width and breadth of the combustion chamber are chosen to be consistent with the distance between the inner and outer wall of the annular burner setup in Refs. [23–25]. Square enclosure geometry was selected over cylindrical geometry in order to more closely resemble the annular confinement using a simple geometric design suitable for a single flame.

In order to generate the acoustic forcing, an excitation signal was created with an Aim-TTi TGA1244 signal generator and amplified by a TQX PRO1000 amplifier before being sent to the horn drivers. To characterize the excitation the inlet tube is equipped with two pressure ports, which are 46 mm and 110 mm upstream of the dump plane, respectively. Each port is equipped with a Kulite XCS-093-0.35D pressure transducer flush mounted with the inner wall, and the signal from these transducers is amplified using a Fylde FE-579-TA bridge amplifier. The two-microphone method [26] was used to relate pressure fluctuations to velocity fluctuations. To aid the reconstruction of the acoustic perturbations, especially for low forcing frequencies, a Dantec 55P11 hotwire was inserted in the injector pipe approximately 77 mm upstream of the dump plane.

A Phantom v2012 high-speed camera with a LaVision intensified relay optics unit and a Hamamatsu photomultiplier (*H11902-113*) and amplifier (*C7169*) are used to measure the local and global OH* chemiluminescence, respectively. Both are equipped with identical bandpass filters centered at 310nm, with a full width half maximum of 10nm. The camera is equipped with a Cerco 2178 UV lens. Images were acquired over a period of 1s at a sampling rate of 10kHz. The images from the side and top views have resolutions of 11.4 pixel/mm and 8.3 pixel/mm, respectively.

The photomultiplier signal is logged together with the pressure and forcing reference signal using NI-9234 24-bit DAQ (Austin, TX) cards at a sampling frequency $f_s = 51.2$kHz. A constant sample length of 10 s was used in order to capture the response at each condition. A range of operating conditions were investigated, varying both the equivalence ratio, $\Phi = 0.6 - 1.0$, and the bulk inlet velocity, $U_b = 12 - 20$ m/s. This allowed us to investigate the flame response over a similar range of operating conditions to previous instability studies in annular geometry [23,24].

Theoretical Approach

Flame Transfer Function. The aim of this study is to characterize and understand the flame response to inlet velocity oscillations. We approach this using the well-known framework of the flame transfer function [7,8,14,24–29]. The flame transfer function can be defined in frequency space as

$$\mathrm{FTF}(\omega) = \frac{\langle \dot{q}' \rangle / \overline{\langle \dot{Q} \rangle}}{u'/U_\mathrm{b}} \tag{1}$$

where $\langle \dot{q}' \rangle$ and u' are the respective amplitudes of the global heat release rate fluctuations and acoustic velocity perturbations in frequency space, and $\overline{\langle \dot{Q} \rangle}$ and U_b are the mean heat release rate and the mean axial bulk exit velocity, respectively. The heat release rate is assumed to be directly proportional to the OH* chemiluminescence signal due to the use of a perfectly premixed air-fuel mixture [29], and the effect of heat losses to the wall are neglected. The frequency space amplitudes of the heat release rate oscillations in Eq. (1) are computed by dividing the recorded signal into 40 segments with 50% overlap and evaluating the cross power spectral density with the forcing signal to reduce the effect of background noise. Additionally, Hann windowing was employed to reduce finite signal length effects.

The two microphone method is used to evaluate the velocity oscillation amplitude [26]. In a long narrow tube with a mean flow, the pressure mode is assumed to be two one-dimensional plane waves propagating in opposite lengthwise direction. Mathematically, this is expressed as $p(x,t) = (A_+ e^{-\mathrm{i}k_+ x} + A_- e^{\mathrm{i}k_- x}) e^{\mathrm{i}\omega_0 t}$, where subscript + and – denote downstream and upstream propagating components, respectively. $A_\pm$ are complex amplitudes, $k_\pm$ are the corresponding wave numbers, x is the location along the tube, ω_0 is the dominant angular frequency in the signal and t is the time. The wave numbers are related by $k_\pm = k_0/(1 \pm M)$ where k_0 is the wave number in the absence of a mean flow, and M is the mean flow Mach number.

The acoustic velocity perturbation corresponding to the pressure fluctuations is [26]

$$u(x,t) = \left(A_+ e^{-\mathrm{i}k_+ x} - A_- e^{\mathrm{i}k_- x}\right) \frac{e^{\mathrm{i}\omega_0 t}}{\rho c} \tag{2}$$

Here, ρ is the mean fluid density and c is the mean speed of sound in the injector tube. $A_\pm$ can be calculated by the two microphones in the injector only, but the direct velocity fluctuation measurements in the tube are also used to make a least squares solution of $A_\pm$, in order to reduce uncertainty.

The flame response was characterized over a wide range of excitation frequencies, $f_0 = 50 - 2000$ Hz, in steps of 50 Hz, in order to cover a typical Strouhal number range [8]. In comparison with previous studies [6–9], the frequencies of interest in this study are relatively high, due to the small physical size of the inlet and combustor geometry, and the high velocities used in previous studies of this injector configuration in annular chambers [23,24]. The acoustic excitation was adjusted at each frequency of interest in order to maintain a constant amplitude of $u'/U_\mathrm{b} = 0.05 \pm 0.01$, permitting evaluation of the linear response at the chosen operating conditions for the frequencies of interest.

In the current investigation, the flame response will be described in terms of the acoustic velocity perturbations evaluated at a reference location corresponding to the combustor inlet or dump plane. The dump plane is chosen as the reference location due to the acoustic mode which is setup in the injector tube, which causes the acoustic velocity oscillations at the combustor inlet to dominate the FTF, if the convective perturbations from the swirler are neglected. As this location is directly downstream of the swirler, additional convective perturbations may be present in the total velocity oscillations at the combustor inlet, which are not taken into account through this definition, which is based solely on the upstream measurement of pressure. However, this definition is chosen to be suitable for direct input into low-order models, allowing the swirler and flame response to be lumped together in a single response function. It should also be noted that due to the close proximity of the swirler to the exit plane, if the reference location for the acoustic velocity perturbations was instead chosen to be just upstream of the swirler, very similar gain and phase values would be observed for the majority of frequencies of interest.

Distributed Time Lag Models. Another aim of this work is to examine if the flame transfer function can be accurately described using a DTL approach, which permits the flame response to be modeled as series of time delays which have different characteristic gains, phases and delays. The application of such a model in this study provides additional insight into the response of the system through the fitted model constants of interest and also allows the transfer functions reported here to be accurately reconstructed for deployment in low-order models.

In this study, the distributed time lag expression introduced by Æsøy et al. [16] for nonswirling flames will be used. The total distribution $\mathrm{DTL_T}$ is given by

$$\mathrm{DTL_T}(\omega) = \exp(-\mathrm{i}\phi_0) \sum_{i=1}^{2} \left(E_i^+(\omega) + E_i^-(\omega)\right) \tag{3}$$

$$E_i^\pm = \frac{g_i}{2} \exp\left[-\frac{1}{2}(\omega \pm \beta_i)^2 \sigma_i^2 - \mathrm{i}\omega\tau_i\right] \tag{4}$$

where ϕ_0 is a phase common to all the components of the distribution. This formulation corresponds to a Gaussian Impulse Response with a cosine modulation in the time domain, allowing for excess gain for a single time delay distribution. In Eq. (4) the maximum value of each Gaussian is given by $g_i/2$, β_i is the angular frequency of the modulation term, σ_i determines the width of the Gaussian and τ_i is the characteristic delay between the acoustic perturbation and the heat release rate response. $E_i^\pm$ corresponds to a Gaussian distribution centered at $\mp\beta_i$, making the magnitude of each distribution, DTL_i, symmetric around $\omega = 0$.

Equation (3) can describe any phenomenon where there are two distinct time scales, τ_1 and τ_2, in the problem. In the first DTL, representing the FTF without modulations caused by the swirler, β_1 corresponds to the frequency of maximum excess gain (gain above unity), which in combination with σ_1 gives the cutoff frequency of the low-pass behavior of the FTFs. The time delay τ_1 represents the convection time from the dump plane to the flame. The interpretation of the second DTL model is slightly different, where β_2 is the preferred frequency of the formation of convective perturbations by the swirler. σ_2 determines the width of the frequency range where the swirler produces significant perturbations, and depending on the value of β_2 and σ_2 it can either be a low-pass or a bandpass behavior. The associated time delay τ_2 is the total convective time from perturbation is created at the swirler until it reaches the flame.

According to theory, there is a unit gain in the low frequency limit [30], introducing the constraint

$$|\mathrm{DTL_T}(\omega = 0)| = 1 \tag{5}$$

on Eq. (3). In practice, this is imposed by letting g_1 be a function, $g_1(g_2, \beta_1, \sigma_1, \beta_2, \sigma_2)$, of the other parameters. It would also be possible to express g_2 as a function, but g_1 is preferred for numerical reasons. Another physical constraint in the low frequency limit is the phase of the FTF should be zero, but this constraint is relaxed by the introduction of ϕ_0 in Eq. (3). This is done to account for any phase discrepancy created by the acoustic mode reconstruction due to uncertainty in the position and the finite size of the microphones. Additionally, it improves the overall fitting of the large range of function parameters, by reducing the effective weighting of the overall regression on this phase condition.

A modulation in the flame response is captured by the two components, $i = 1, 2$, causing positive and negative interference. The wavelength in frequency space of the modulation is controlled by the inverse of the difference in time delays, $\lambda = 1/\tau_3 = 1/(\tau_2 - \tau_1)$. The phase difference at the dump plane for low Mach number flows is given by $\Delta\phi \approx 2\pi f L_\mathrm{swirler}/U'_\mathrm{bt}$ [13,31], where $L_\mathrm{swirler}/U'_\mathrm{bt}$ is the mean convective time delay between the swirler trailing edge and the dump plane. The first minima in FTF gain is expected at $\Delta\phi = \pi$, meaning the

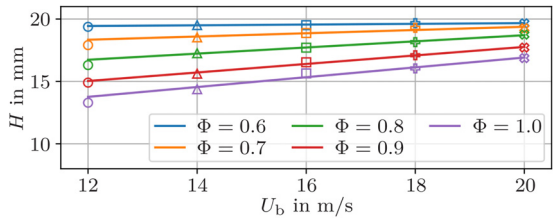

Fig. 2 Vertical flame height over a range of equivalence ratios, Φ, and bulk exit velocities, U_b. Measured flame heights are represented by markers, and the solid lines represent linear regressions. (Color online).

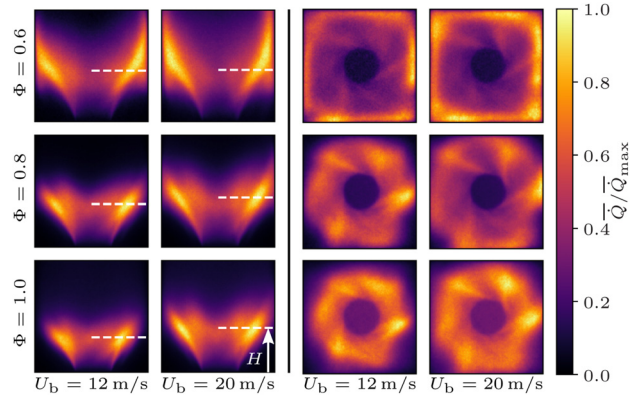

Fig. 3 Side (*left*) and top (*right*) view of average unforced flame shape with equivalence ratio Φ (*vertical axis*) and bulk inlet velocity U_b (*horizontal axis*). Distributions are cropped at the combustion chamber extremities. The white dashed line in the side views indicates the measured vertical flame height *H*. (Color online).

wavelength in frequency space, λ, is determined solely by the distance between the two sources of time delays and the convective velocity for low Mach number flows. The larger the difference in time delays, the sharper the modulations will appear in the FTF, in other words the dip will be narrower and affect a smaller range of frequencies.

Results and Discussion

Unforced Flames. An important scaling parameter for response is the flame height H, defined as the streamwise location of the maximum cross-stream integrated heat release rate of the unforced flames, and is shown for all operating conditions in Fig. 2. Assuming negligible changes to the turbulent flame speed for increasing bulk velocity in the studied interval, the flame height is expected to scale linearly with bulk velocity at a fixed equivalence ratio [29]. The solid lines in Fig. 2 are linear regressions based on the different bulk velocities, showing good agreement between measured and expected behavior. For increasing bulk velocity, the flames elongate due to the decreasing ratio of flame speed to bulk velocity, while for increasing equivalence ratio the flames shorten due to the increase in flame speed.

A selection of flame shapes are shown through line of sight integrated images from the side and top of the flame in Fig. 3. For all operating conditions, the flame structure resembles that of a V-flame, but with some flame elements stabilized in the outer shear layer. The side view shows the same flame height trends observed in Fig. 2, with increasing flame height when either increasing the bulk velocity or decreasing the equivalence ratio. When $\Phi = 0.6$, the flame attaches to the side walls of the combustion chamber, which is also clearly seen from the top view. This causes an underestimation of the flame height due to the spatial redistribution of heat release rate, as seen in the side views in Fig. 3.

The other operating conditions in Fig. 3 show less flame wall interaction. However, a secondary inner structure can be observed inside the main reaction zone from the side views. This can be further examined from the top views, where a clear six-fold rotational symmetry is observed. This is caused by the close proximity of the six vane swirler to the dump plane combined with the relatively large blockage presented by the swirler. Despite the very thin vanes (thickness of 1mm), the high inclination angle of $\alpha = 60$ deg results in a relatively high blockage, producing notable wakes, which are likely causing the secondary structure. Such features associated with this geometry have been observed previously [23], but can be viewed here in higher resolution.

Flame Transfer Function Scaling. Flame transfer functions for all operating conditions are presented in Fig. 4. Adopting a similar scaling to a number of previous investigations [6,32,33], the gain and phase are plotted against a Strouhal number, $\mathrm{St}_1 = fH/U_b$. The FTF gain for all cases exhibits a low-pass filter behavior which is well documented for acoustically perturbed flames [6,29,34] for Strouhal numbers $\mathrm{St}_1 \gtrsim 1$, showing a reasonable collapse in both gain and phase for constant Φ, but less agreement as equivalence ratio is varied. However, despite modest variations in gain and phase, at high St_1 similar cutoff behavior is observed. The onset of cutoff occurs at slightly lower values of St_1 for $\Phi = 0.6$, but this is most likely caused by an underestimation of flame height due to wall attachment of the flame, shown in Fig. 3. This observation is further supported by the steeper evolution of the phase compared to the other equivalence ratios. Plotting the transfer function variation with St_1 is equivalent to scaling the response with the dominant time scale, explaining the almost linear slopes of the phase. It is noted that when $\mathrm{St}_1 \gtrsim 1.5$ the slope of the $\Phi = 0.6$ drastically changes shape. This coincides

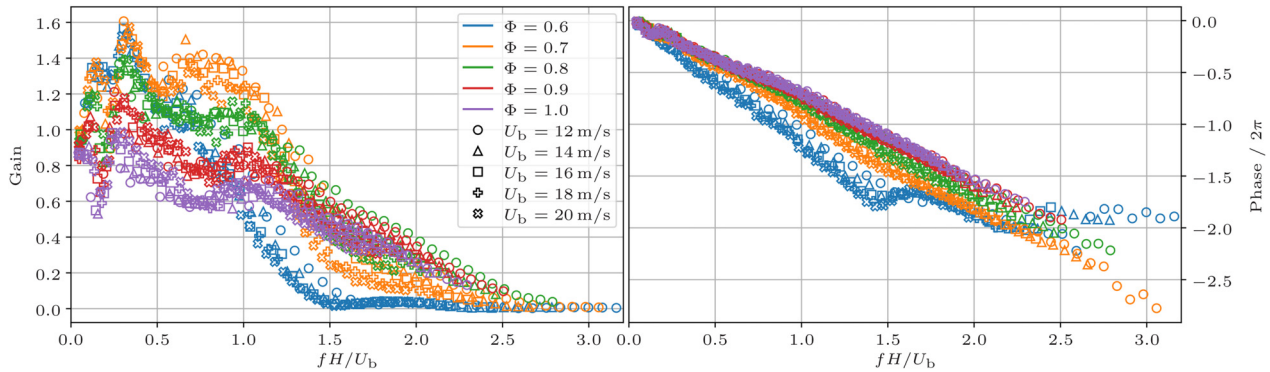

Fig. 4 Flame response in terms of the flame transfer function gain (*left*) and phase (*right*) for all cases, normalized by Strouhal number St_1. Colors and symbols are consistent with those used previously in Fig. 2 for flame height. (Color online).

with a very low gain value, meaning measurement noise and any potential extra time delays may result in a major change in the phase.

In contrast, however, at low St_1 the transfer function gain does not collapse and is observed instead to significantly decrease with increasing equivalence ratio, creating a local minima or dip at $St_1 \approx 0.75$ when $\Phi \geq 0.8$. Similar dip features have been observed in previous studies of highly swirling flames [6–9], which are attributed to the interference between convective and acoustic velocity perturbations at the dump plane [8]. The presence of multiple time scales associated with such interference phenomena can also be observed through the subtle changes of the phase slope in Fig. 4 for the high equivalence ratio cases.

It is noted that there are some non-negligible modulations for very low Strouhal numbers ($St_1 < 0.3$), but these will later be shown to likely stem from a source of convective perturbations upstream of the swirler due to the wavelength λ in frequency space. However, the main focus of this study will relate to the suppression of the expected dip caused by the swirler for decreasing equivalence ratio. For a given inlet velocity, the hydrodynamic and acoustic response in the inlet duct should be approximately the same for all equivalence ratios due to the same bulk velocity and negligible changes in density. Therefore, the absence of interference at $St_1 \approx 0.75$ for some equivalence ratios is somewhat unexpected and will be studied further in the flame dynamics section.

Alternative Strouhal Number Scaling. The St_1 scaling in Fig. 4 is designed to collapse the cutoff frequency of the FTF, but the location of the minima clearly observed for $\Phi \geq 0.8$ is expected to scale with another Strouhal number. This Strouhal number is based on the convective time from the swirler to the dump plane of the induced perturbations and is given by $St_3 = fL_{swirler}/U'_{bt}$, with the rescaled FTFs in Fig. 5. In this scaling, it is assumed the convective time from the swirler to the dump plane is proportional to the time it takes for a disturbance to travel, at the local bulk velocity U_{bt} (which varies with cross-sectional area). Recently, it has been shown by Albayrak et al. [35] that the propagation speed of the perturbation created at the swirler is significantly faster than U_{bt} due to its inertial wave nature. Therefore the propagation speed in St_3 is estimated to be $U'_{bt} = 1.5U_{bt}$ based on the theoretical dip location $St_3 = 1/2$ and visual inspection of Fig. 5. Using this scaling, the length of the modulation should be unity and the frequency location of the dips collapse as shown in the figure. While the dip frequency locations collapse reasonably well for the previous St_1 scaling shown in Fig. 4, this is due to the flame heights' weak dependence on the inlet velocity for a given equivalence ratio.

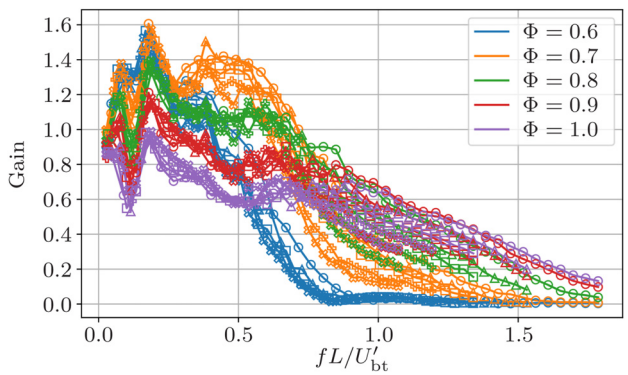

Fig. 5 Flame response in terms of the flame transfer function gain (*left*) and phase (*right*) for all cases, normalized by Strouhal number St_3. Colors and symbols are the same as presented in Fig. 4. (Color online).

The modulations at the lowest Strouhal numbers $St_3 \lesssim 0.2$ interestingly also collapse well. The much shorter wavelength in frequency space of these suggests a source of convective vorticity oscillations upstream of the swirler. A likely source of the extra convective perturbations is the grub screws used upstream to center the bluff body, the same source as described in detail in Ref. [16]. The visual effect of these low Strouhal number perturbations on the flame is very subtle even in the absence of swirl, and therefore in the presence of additional perturbations induced by the swirl vanes, it was decided not to examine the effect of these further.

The similarity of the time scales represented by the two Strouhal numbers St_1 and St_3, with τ_1 in the range $0.85 - 1.62$ ms, and τ_3 in the range $0.53 - 0.89$ ms, results in several interesting features. One prominent feature is the frequency location of the dip being located close the cutoff region, and in some cases extending all the way until cutoff starts to dominate. This results in the local maximum following the dip not being present in all cases. Compared to previous studies [8,14], the location of measured maximum interference is very high, in the range $0.5 - 0.9$ kHz, and the width of the dip in frequency space is much broader.

Distributed Time Lag Models. Examining the gain and phase of the flame response over the range of presented cases shows that the response can either be dominated by the time lag based on the flame height, or a significant interference with the convective perturbations created at the swirler can introduce an additional time scale. Therefore, to confirm this, and to gain additional insight into these characteristic values a distributed time delay model [17] is employed, with either a single or a pair of time delays used.

The DTL model described in the theory section is applied to the measurements in this study, and the reconstructed functions for each case are shown in Fig. 6. In this study, the potential third convective time lag is not considered, and therefore the range used for the parameter fitting starts at $f_0 = 300$ Hz and will not capture the first sharper dip by design. For presentation clarity, a

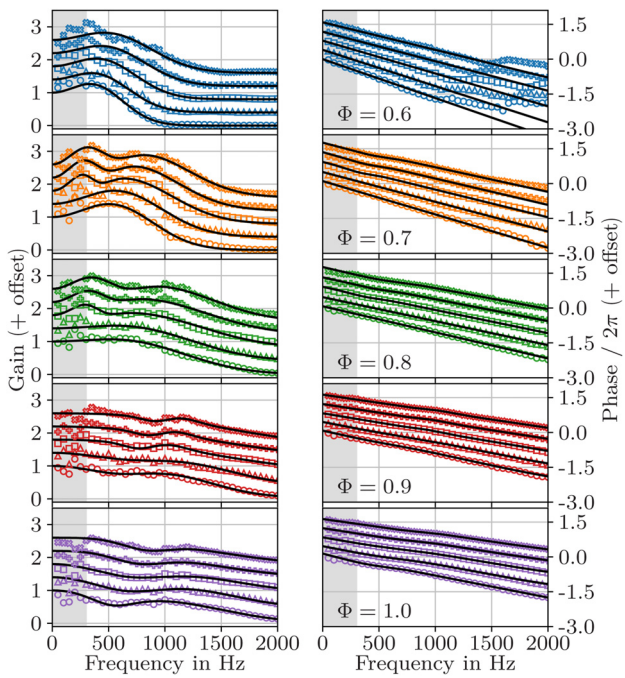

Fig. 6 FTFs and fitted distributed time delay model, with one ($\Phi = 0.6$ and $U_b = 12-14$ m/s for $\Phi = 0.7-0.8$) or two (otherwise) time delays. The colors and markers are the same Fig. 4. Both the phase and gain curves are offset by 0.4 for each increase in velocity to aid readability. (Color online).

positive offset of 0.4 has been added to both gain and phase for increasing velocity in order to separate the functions, and these are plotted now against frequency to allow a compact presentation of all 25 cases. The parameters presented can be found in Appendix A (Table 1).

Corresponding to previous observations, a single DTL is used when $\Phi = 0.6$ for all velocities, and for $\Phi = 0.7 - 0.8$ when $U_b = 12 - 14\,\mathrm{m/s}$. For the single time delay cases with $\Phi = 0.7 - 0.8$ the width and amplitude of the dip is too small and the location is too close to the 300 Hz cutoff point to fit the model well, but the single delay captures the main features well. For all other cases, two delays are used to capture the features of the transfer function. The close agreement between measurements and the fitted model for all cases indicates that this modeling approach is appropriate, including the use of only a single time delay for the low equivalence ratio cases with $\Phi = 0.6$.

To study the reconstruction further, the aforementioned coefficients are graphically presented in Fig. 7. First the time delays are examined, which are shown on the bottom row. There is good agreement between the fitted time delays and the theoretical values from the Strouhal number scaling. The first time delay τ_1 scales with the ratio of flame height H to the bulk velocity, while the second time delay τ_2 is a sum of τ_1 and the convective time from the swirler to the dump plane. This implies that the shorter time delays due to the dispersive inertial wave nature of the convective perturbations from the swirler are automatically accounted for in the fitted model values of τ_2, and therefore the fitted time delay is the one best characterizing the actual time delay. For τ_1 it is observed that the high equivalence ratio cases, which correspond to short flame heights, overestimate the time delay, suggesting the definition of the time delay is slightly incorrect for these cases. It is also observed that as the flame length increases, the time scale is underestimated. This may be explained by the underestimation of the flame height H observed previously, when the flame begins to interact with the wall. It also shows the model, which was originally proposed for unswirled flames [16], is capable of recreating the response well with a very simple expression suitable for modeling and based on the assumption of two distinctive time scales in the problem.

In terms of the other model parameters, the first DTL distribution is also observed to always behave as a low-pass filter, in line with the expected behavior of a perfectly premixed flame. Observing g_1, β_1, and σ_1 in Fig. 7, there are clear trends for the evolution of the parameters for the first DTL as a function of equivalence ratio. As the equivalence ratio is increased both the location β_1 of the maximum gain and the width σ_1^{-1} increases, resulting in a simultaneous decrease in the gain g_1 due to the symmetry of Eq. (3).

However, the other model parameters for the second DTL do not show such clear trends, due to the under-constrained fitting and the much lower amplitude of the phenomenon. This causes the interpretation of the swirler behavior to not be physically consistent across all cases, despite the models ability to accurately describe the transfer function in the region of interest $f_0 = 300 - 2000\,\mathrm{Hz}$. The second DTL is observed to either be a bandpass filter centered at a high frequency, $\beta_2 > 700$ Hz, or a bandpass to low-pass filter with finite amplitude at zero frequency, $\beta_2 \lesssim 350\,\mathrm{Hz}$. It is important to note that while the correct time delay τ_2 is reliably captured, the type of filter is not consistent across all cases.

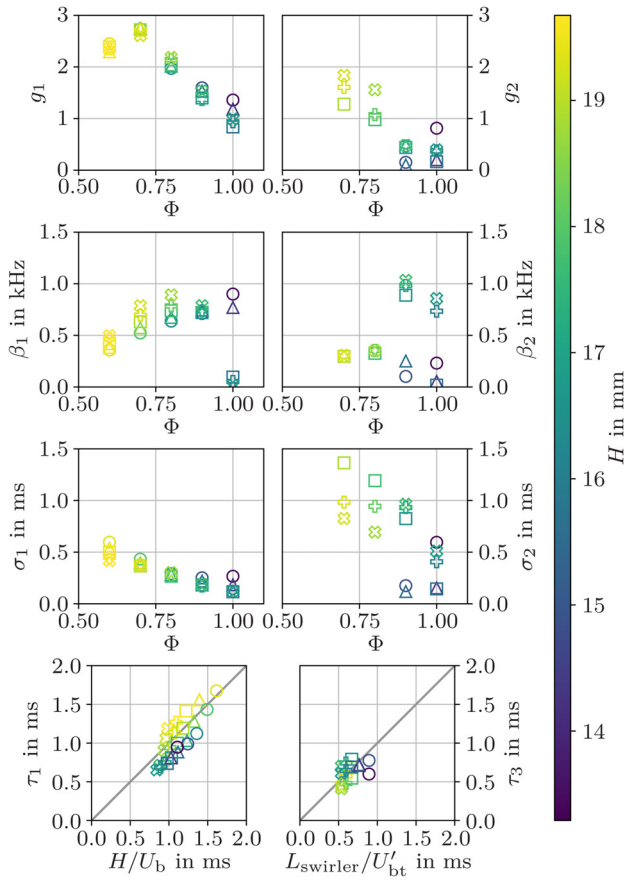

Fig. 7 Parameters for DTL$_1$ (*left*) and DTL$_2$ (*right*) for all operating conditions. $g_{1,2}$, $\beta_{1,2}$ and $\sigma_{1,2}$ are plotted against equivalence ratio and the time delays $\tau_{1,3}$ are plotted against the respective Strouhal number time delays. The color indicates the flame height H, and the symbols indicate the same velocities as in previous figures. (Color online).

Phase Averaged Flame Dynamics. In order to further understand the spatial location, magnitude, and phase of the heat release rate oscillations, the phase averaged heat release rate distribution is presented for two operating conditions at select frequencies. Two extremes are chosen in terms of the peak magnitude of the FTF response, with the $\Phi = 0.7$, $U_b = 18\,\mathrm{m/s}$ case presented in Fig. 8, and the $\Phi = 1.0$, $U_b = 12\,\mathrm{m/s}$ case presented in Fig. 9. The frequencies presented correspond to a location before the expected local minimum, a frequency close to expected local minimum of the dip and a third higher frequency. For the $\Phi = 0.7$ case the highest frequency is well into the cutoff range, while it is at the local maximum after the dip for $\Phi = 1.0$. The forcing amplitude is adjusted to $u'/U_b = 0.1$ to better highlight the flame dynamics.

For the selected forcing frequencies, the weighted phase representation [36] of the first Fourier mode of the phase average (*left*) and five points in the phase averaged cycle are presented from both the side and top views (*center*). In the weighted phase representation, the brightness and color are determined by the fluctuation magnitude and phase, respectively, on a pixel by pixel basis. On the right-hand side, the integrated response of the first Fourier mode is plotted over two periods to show the timing of the heat release rate in the streamwise direction, which is a similar metric to the phase averaged representation presented in fig. 14 in Ref. [8]. The complex amplitude $\tilde{\dot{q}}'_y(x)$ is found by first integrating the heat release rate in the transverse direction (y-direction in Fig. 1(*a*)), and then taking the discrete Fourier transform of the integrated heat release rate at the forcing frequency f_0. The presented time series of the first Fourier mode is then given by $\Re(\tilde{\dot{q}}'_y e^{i2\pi t/T})$ normalized by the mean spatially integrated heat release rate. The time series are plotted against downstream distance, x, in order to create contour maps of the first Fourier mode, in which streaked regions represent the convection of high and low oscillations in space and time. The mean value along a horizontal cut represents the quantity $\langle q' \rangle / \overline{\langle \dot{Q} \rangle}$ in Eq. (1).

Considering initially the low equivalence ratio case ($\Phi = 0.7$, $U_b = 18\mathrm{m/s}$) in Fig. 8, for each forcing frequency the

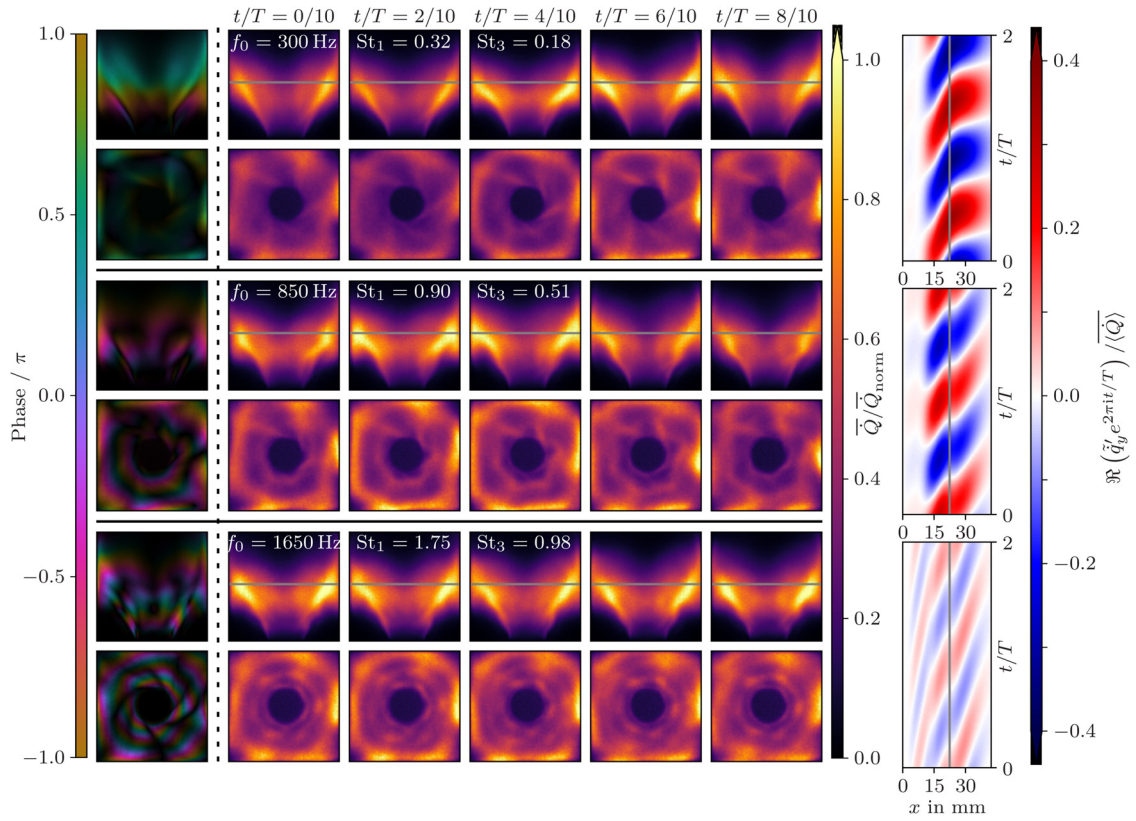

Fig. 8 Weighted phase (*left*), phase averages (*center*), and the time evolution of the cross integrated first Fourier mode (*right*) for different forcing frequencies, f_0. The weighted phase plots and the phase averages are presented from both the side and top view. All operating conditions are at a bulk velocity $U_b = 18$ m/s and equivalence ratio $\Phi = 0.7$. $\overline{\dot{Q}}_{norm} = 0.9\overline{\dot{Q}}_{max}$ to slightly saturate the plots for viewing clarity. (Color online).

phase averaged motion of the flame in response to the velocity oscillations can be observed. The side view shows the flame front oscillating as perturbations convect along it, rolling up the flame brush at the tip. During the cycle, the flame tip remains attached to the combustion chamber walls. The top view confirms that flame wall interactions are present throughout the cycle, but also provides insight into the asymmetry of the heat release structure. This view shows fluctuations traveling along the flame front as hexagonal ring structures, with this patternation due to the close proximity of the swirler to the dump plane. The number of ring structures increase with frequency as the wavelength of the convective perturbation decreases. The effect of this can also be observed in the side view, with the flame oscillating less for the highest frequency.

The features observed in the phase averaged distributions can be described more compactly through the weighted phase plots shown on the left-hand side of Fig. 8. The two lower frequency cases, $f_0 = 300$ Hz and $f_0 = 850$ Hz, experience most heat release rate oscillations in the upper part of the flame, close to the walls. Furthermore, the range of phase angles present for the two lower frequencies are restricted to a span of approximately half a period, indicating that no significant destructive interference is occurring in these cases. In contrast, the highest frequency case, $f_0 = 1650$ Hz, contains similar magnitude oscillations at all downstream locations. Together with the shorter convective disturbance wavelength at the higher frequency, this results in a wider range of oscillation phases. The presence of significant amplitude oscillations at phase angles separated by a full period in this case provides the destructive interference consistent with the response in the cutoff region.

While the weighted phase plots provide a useful way to compactly represent the structure of the oscillations in heat release rate, in order to further understand the interference between convective perturbations it is instructive to examine first Fourier mode contour plots on the right-hand side of Fig. 8. Due to the normalized time axis, the inclination angle of the streaked blue and red regions (which represent the convection of positive and negative heat release rate oscillations) with respect to the horizontal is controlled by both the advection velocity along the flame and the frequency. For a fixed inlet velocity and equivalence ratio, the advection velocity is expected to remain relatively constant, resulting in a monotonically increasing streak angle with frequency.

Frequency $f_0 = 850$ Hz in Fig. 8 corresponds to a case where significant destructive interference may be expected ($St_3 \approx 0.5$), but as shown in Fig. 4, this is not observed for equivalence ratio $\Phi = 0.7$. A crucial observation from the first Fourier mode plot in Fig. 8 is the occurrence of a significant temporal shift in the streaks at a downstream location $x \approx 22$ mm, which is marked with a gray line. This temporal shift manifests in the contour plots as a sharp decrease in the inclination angle of the streaked regions at this downstream location. Such a temporal shift increases the magnitude of the heat release oscillations, by reducing the expected level of interference. This can be understood by considering the average heat release rate oscillations along any horizontal cut in the first Fourier mode plot. The sharp decrease in streak angle results in less cancelation of heat release rate oscillations. Therefore, the absence of the expected minima at $St_3 \approx 0.5$ is likely caused by this temporal shift resulting in less interference.

In the absence of confinement, it is reasonable to assume the convective velocity along the flame should vary gradually with downstream location. Therefore, it is interesting to compare the downstream location of the clear shift in the Fourier mode timing to the phase averaged representation in the center of Fig. 8, also marked with gray lines. The downstream location of the shift corresponds to approximately the mean height of the flame-wall

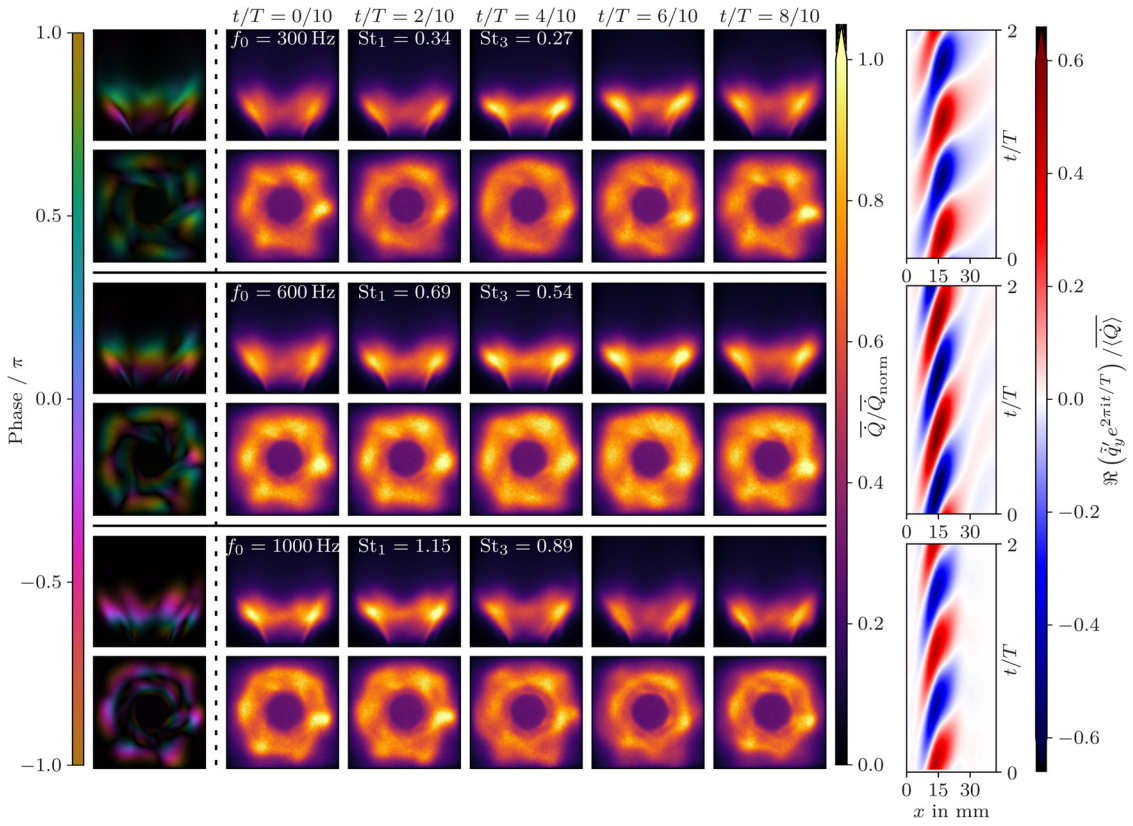

Fig. 9 Weighted phase (*left*), phase averages (*center*) and the time evolution of the cross integrated first Fourier mode (*right*) for different forcing frequencies, f_0. The weighted phase plots and the phase averages are presented from both the side and top view. All operating conditions are at a bulk velocity $U_b = 12$ m/s and equivalence ratio $\Phi = 1.0$. $\bar{\dot{Q}}_{\mathrm{norm}} = 0.9\bar{\dot{Q}}_{\mathrm{max}}$ to slightly saturate the plots for viewing clarity. (Color online).

impingement during the cycle, suggesting that the flame confinement is the main cause of the change in streak angle, and consequently the suppression of interference. Therefore, the presence of confinement explains the absence of the dip feature for this equivalence ratio case. Returning to the Fourier mode distribution, the decrease in streak angle suggests the suppression is realized through a modification of the convective velocity. Furthermore, as the intensity of the heat release rate oscillations are similar before and after this location, it appears that neither quenching nor a modification of the flame-vortex interaction due to the presence of the wall is the dominant mechanism for the interference suppression.

Figure 9 shows the same metrics as Fig. 8 for a case with significant interference observed in the FTF gain ($\Phi = 1.0$ and $U_b = 12\,\mathrm{m/s}$). An important difference in comparison with Fig. 8 is the flame is significantly shorter, and hence, does not interact strongly with the wall, as seen from the phase averaged cycle. Therefore, despite the use of the same enclosure geometry, through the variation of operating conditions, the effective confinement is reduced. At $f_0 = 300$ Hz more fluctuations close to the flame base are visible in the $\Phi = 1.0$ case in comparison with the lower equivalence ratio, giving a wider range of phases. However, the top view shows the high-magnitude oscillations occur in the upper section of the flame, with a narrow range of phases dominating, similar to the $\Phi = 0.7$ case.

It is interesting to contrast this response with the weighted phase plots from the $f_0 = 600$ Hz case, which corresponds to the local FTF interference minima. At this higher frequency, a relatively wide range of phases can be seen from the side and now also from the top view, demonstrating the presence of multiple disturbances on the flame at the same instances, and therefore the cancelation of integrated heat release rate oscillations. This can be clearly observed in the cross integrated Fourier modes where regions of positive and negative heat release rate oscillation are simultaneously present. Crucially, in this case the temporal shift of the streaks only occurs after the peak heat release rate oscillations occur, and thus a greater amount of cancelation is present, resulting in the observation of the expected local FTF minimum at the frequency predicted by theory. Therefore, the absence of close wall confinement due to the shorter flame height allows destructive interference to occur in this case.

Comparing cases corresponding to the local FTF maximum at $f_0 = 1000$ Hz to the local FTF minimum at $f_0 = 600$ Hz, a narrower range of phases in the weighted phase plot is observed for the former. This is also shown in the cross integrated Fourier mode plot in which a lower response is observed both toward the flame base and toward the top of the flame. Therefore, as oscillations at this frequency result in heat release rate oscillations at a narrower range of heights, less interference is observed, corresponding to the local maxima in the transfer function.

Conclusion

The FTF of a closely confined, swirling flame have been investigated experimentally for a wide range of operating conditions. The FTFs are shown to exhibit characteristic low-pass behavior and collapse reasonably well when plotted nondimensionally against a Strouhal number based on the flame height and bulk flow velocity. Further to this, at high equivalence ratios $\Phi \geq 0.8$ the FTF is observed to have characteristic modulations in both the gain and phase typically associated with highly swirling flames. These are caused by the interference between convective perturbations from the swirler interacting with the perturbations at the injector exit. This is confirmed by scaling the FTFs against a second Strouhal number based on the upstream swirler location and the convective velocity in the inlet pipe. Due to the small length

scales and relatively high velocity in the studied configuration, the frequency of the dip in the gain is relatively high compared to other studies, and it spans a much wider range of frequencies, which is consistent with the current understanding of the phenomenon.

However, in contrast to previous studies, at the lower equivalence ratios $\Phi \leq 0.7$ the expected modulations due to convective perturbations from the swirler are shown to be suppressed. By examining the flame structure and dynamics, it is shown that at lower equivalence ratios (and higher velocities) the flames are longer and therefore interact significantly with the walls. This increase in effective confinement results in a temporal shift in the heat release distribution at the downstream location where the flame impinges on the wall during the oscillation cycle. The temporal shift reduces the interference between convective perturbations from the swirler and from the injector exit for a given frequency due to an increase in convective velocity, which increases the FTF gain compared to the higher equivalence ratios with smaller effective confinements. This demonstrates the response is not only dependent on the hydrodynamic and acoustic oscillations at the inlet, but also on the downstream effective confinement.

Finally, to gain additional insight into the time scales of the problem a DTL model with two distinct time scales is applied to the FTFs. The model is shown to accurately capture the time delays as well as providing a simple expression for recreating and interpolating the FTF. The extracted time delays correctly capture the fact that the convective time delay from the swirler to dump plane is faster than the local bulk velocity, due to the inertial wave nature of the perturbations, as well as demonstrating the difficulty in defining the flame height for flames attached to the combustion chamber walls.

Funding Data

- European Research Council (ERC) under the European Union's Horizon 2020 (Grant No. 677931 TAIAC; Funder ID: 10.13039/100010663).

Appendix A

The coefficients for all the DTL models presented in Fig. 6 are presented in Table 1. As discussed the fitting does not account for the effect possibly caused by a third convective time lag in the model, and is therefore not applicable to recreate that behavior. The quality of the fit can be checked in Fig. 6.

Table 1 Coefficients used for creating the modeled FTFs as shown in Fig. 6

Φ	U_b in m/s	H in mm	g_1	$\beta_1/(2\pi)$ in Hz	σ_1 in ms	τ_1 in ms	g_2	$\beta_2/(2\pi)$ in Hz	σ_2 in ms	τ_2 in ms	ϕ_0
0.6	12	19.4	2.450	358	0.596	1.675	N/A	N/A	N/A	N/A	0.000
0.6	14	19.5	2.294	382	0.537	1.560	N/A	N/A	N/A	N/A	−0.006
0.6	16	19.5	2.389	420	0.500	1.414	N/A	N/A	N/A	N/A	0.017
0.6	18	19.7	2.354	464	0.449	1.269	N/A	N/A	N/A	N/A	0.129
0.6	20	19.7	2.356	498	0.418	1.187	N/A	N/A	N/A	N/A	0.078
0.7	12	17.9	2.737	523	0.432	1.434	N/A	N/A	N/A	N/A	−0.674
0.7	14	18.5	2.751	573	0.395	1.282	N/A	N/A	N/A	N/A	−0.614
0.7	16	18.9	2.722	632	0.366	1.192	1.279	296	1.365	1.875	−0.839
0.7	18	19.3	2.713	695	0.375	1.136	1.605	300	0.984	1.711	−0.963
0.7	20	19.3	2.609	787	0.371	1.059	1.837	307	0.826	1.508	−1.026
0.8	12	16.3	1.972	638	0.291	1.123	N/A	N/A	N/A	N/A	−0.474
0.8	14	17.3	2.013	674	0.279	1.032	N/A	N/A	N/A	N/A	−0.424
0.8	16	17.7	2.039	738	0.266	0.998	0.979	326	1.192	1.546	−0.716
0.8	18	18.2	2.142	785	0.270	0.942	1.076	354	0.944	1.420	−0.759
0.8	20	18.8	2.186	892	0.302	0.906	1.558	352	0.693	1.317	−1.031
0.9	12	14.9	1.597	712	0.251	0.990	0.152	102	0.175	1.766	−0.502
0.9	14	15.6	1.532	746	0.220	0.885	0.102	251	0.118	1.606	−0.331
0.9	16	16.5	1.400	720	0.181	0.810	0.440	889	0.825	1.602	−0.159
0.9	18	17.1	1.370	738	0.171	0.749	0.471	983	0.932	1.493	−0.139
0.9	20	17.7	1.537	788	0.187	0.714	0.480	1033	0.964	1.415	−0.168
1.0	12	13.3	1.360	900	0.266	0.947	0.813	231	0.595	1.547	−0.903
1.0	14	14.4	1.185	770	0.184	0.809	0.201	54	0.153	1.521	−0.379
1.0	16	15.6	0.838	96	0.116	0.737	0.164	18	0.144	1.428	−0.258
1.0	18	16.0	0.936	54	0.120	0.692	0.375	734	0.407	1.339	−0.229
1.0	20	16.9	0.991	13	0.121	0.654	0.395	857	0.510	1.266	−0.190

Note some of the parameters are not qualitatively consistent, which is as previously discussed due to the under-constrained fitting caused by the similar time scales and data range used. However, these coefficients give a quantitatively good fit for recreating the FTFs when $f_0 \geq 300$ Hz, allowing these to be applied in low-order models.

References

[1] Lieuwen, T. C., 2005, "Combustion Instabilities in Gas Turbine Engines," Progress in Astronautics Aeronautics, American Institute of Aeronautics & Astronautics.

[2] Dowling, A. P., 1997, "Nonlinear Self-Excited Oscillations of a Ducted Flame," J. Fluid Mech., **346**, pp. 271–290.

[3] Stow, S. R., and Dowling, A. P., 2004, "Low-Order Modelling of Thermoacoustic Limit Cycles," ASME Paper No. GT2004-54245.

[4] Noiray, N., Durox, D., Schuller, T., and Candel, S., 2008, "A Unified Framework for Nonlinear Combustion Instability Analysis Based on the Flame Describing Function," J. Fluid Mech., **615**, pp. 139–167.

[5] Nicoud, F., Benoit, L., Sensiau, C., and Poinsot, T., 2007, "Acoustic Modes in Combustors With Complex Impedances and Multidimensional Active Flames," AIAA J., **45**(2), pp. 426–441.

[6] Kim, K. T., and Santavicca, D., 2013, "Generalization of Turbulent Swirl Flame Transfer Functions in Gas Turbine Combustors," Combust. Sci. Technol., **185**(7), pp. 999–1015.

[7] Komarek, T., and Polifke, W., 2010, "Impact of Swirl Fluctuations on the Flame Response of a Perfectly Premixed Swirl Burner," ASME J. Eng. Gas Turbines Power, **132**(6), p. 061503.

[8] Palies, P., Durox, D., Schuller, T., and Candel, S., 2010, "The Combined Dynamics of Swirler and Turbulent Premixed Swirling Flames," Combust. Flame, **157**(9), pp. 1698–1717.

[9] Gatti, M., Gaudron, R., Mirat, C., Zimmer, L., and Schuller, T., 2018, "A Comparison of the Transfer Functions and Flow Fields of Flames With Increasing Swirl Number," ASME Paper No. GT2018-76105.

[10] Hirsch, C., Fanaca, D., Reddy, P., Polifke, W., and Sattelmayer, T., 2005, "Influence of the Swirler Design on the Flame Transfer Function of Premixed Flames," ASME Paper No. GT2005-68195.

[11] Schimek, S., Göke, S., Schrödinger, C., and Paschereit, C. O., 2012, "Flame Transfer Function Measurements With CH_4 and H_2 Fuel Mixtures at Ultra Wet Conditions in a Swirl Stabilized Premixed Combustor," ASME Paper No. GT2012-69788.
[12] Straub, D. L., and Richards, G. A., 1999, "Effect of Axial Swirl Vane Location on Combustion Dynamics," ASME Paper No. 99-GT-109.
[13] Kim, K. T., and Santavicca, D. A., 2013, "Interference Mechanisms of Acoustic/Convective Disturbances in a Swirl-Stabilized Lean-Premixed Combustor," Combust. Flame, **160**(8), pp. 1441–1457.
[14] Gatti, M., Gaudron, R., Mirat, C., and Schuller, T., 2017, "Effects of the Injector Design on the Transfer Function of Premixed Swirling Flames," ASME Paper No. GT2017-63874.
[15] Palies, P., Ilak, M., and Cheng, R., 2017, "Transient and Limit Cycle Combustion Dynamics Analysis of Turbulent Premixed Swirling Flames," J. Fluid Mech., **830**, pp. 681–707.
[16] Æsøy, E., Aguilar, J. G., Wiseman, S., Bothien, M. R., Worth, N. A., and Dawson, J. R., 2020, "Scaling and Prediction of Transfer Functions in Lean Premixed H_2/CH_4-Flames," Combust. Flame, **215**, pp. 269–282.
[17] Sattelmayer, T., 2003, "Influence of the Combustor Aerodynamics on Combustion Instabilities From Equivalence Ratio Fluctuations," ASME J. Eng. Gas Turbines Power, **125**(1), pp. 11–19.
[18] Schuermans, B., Bellucci, V., Guethe, F., Meili, F., Flohr, P., and Paschereit, C. O., 2004, "A Detailed Analysis of Thermoacoustic Interaction Mechanisms in a Turbulent Premixed Flame," ASME Paper No. GT2004-53831.
[19] Cuquel, A., Durox, D., and Schuller, T., 2013, "Scaling the Flame Transfer Function of Confined Premixed Conical Flames," Proc. Combust. Inst., **34**(1), pp. 1007–1014.
[20] Birbaud, A.-L., Durox, D., Ducruix, S., and Candel, S., 2007, "Dynamics of Confined Premixed Flames Submitted to Upstream Acoustic Modulations," Proc. Combust. Inst., **31**(1), pp. 1257–1265.
[21] Fu, Y., Cai, J., Jeng, S.-M., and Mongia, H., 2005, "Confinement Effects on the Swirling Flow of a Counter-Rotating Swirl Cup," ASME Paper No. GT2005-68622.
[22] De Rosa, A. J., Peluso, S. J., Quay, B. D., and Santavicca, D. A., 2016, "The Effect of Confinement on the Structure and Dynamic Response of Lean-Premixed, Swirl-Stabilized Flames," ASME J. Eng. Gas Turbines Power, **138**(6), p. 061507.
[23] Worth, N. A., and Dawson, J. R., 2013, "Self-Excited Circumferential Instabilities in a Model Annular Gas Turbine Combustor: Global Flame Dynamics," Proc. Combust. Inst., **34**(2), pp. 3127–3134.
[24] Worth, N. A., and Dawson, J. R., 2017, "Effect of Equivalence Ratio on the Modal Dynamics of Azimuthal Combustion Instabilities," Proc. Combust. Inst., **36**(3), pp. 3743–3751.
[25] Nygård, H. T., Mazur, M., Dawson, J. R., and Worth, N. A., 2019, "Flame Dynamics of Azimuthal Forced Spinning and Standing Modes in an Annular Combustor," Proc. Combust. Inst., **37**(4), pp. 5113–5120.
[26] Seybert, A. F., and Ross, D. F., 1977, "Experimental Determination of Acoustic Properties Using a Two-Microphone Random-Excitation Technique," J. Acoust. Soc. Am., **61**(5), pp. 1362–1370.
[27] Dowling, A. P., 1999, "A Kinematic Model of a Ducted Flame," J. Fluid Mech., **394**, pp. 51–72.
[28] Ducruix, S., Durox, D., and Candel, S., 2000, "Theoretical and Experimental Determinations of the Transfer Function of a Laminar Premixed Flame," Proc. Combust. Inst., **28**(1), pp. 765–773.
[29] Schuller, T., Durox, D., and Candel, S., 2003, "A Unified Model for the Prediction of Laminar Flame Transfer Functions: Comparisons Between Conical and V-Flame Dynamics," Combust. Flame, **134**(1–2), pp. 21–34.
[30] Polifke, W., and Lawn, C., 2007, "On the Low-Frequency Limit of Flame Transfer Functions," Combust. Flame, **151**(3), pp. 437–451.
[31] Palies, P., Durox, D., Schuller, T., and Candel, S., 2011, "Acoustic–Convective Mode Conversion in an Aerofoil Cascade," J. Fluid Mech., **672**, pp. 545–569.
[32] Fleifil, M., Annaswamy, A. M., Ghoneim, Z., and Ghoniem, A. F., 1996, "Response of a Laminar Premixed Flame to Flow Oscillations: A Kinematic Model and Thermoacoustic Instability Results," Combust. Flame, **106**(4), pp. 487–510.
[33] Wang, H., Law, C. K., and Lieuwen, T., 2009, "Linear Response of Stretch-Affected Premixed Flames to Flow Oscillations," Combust. Flame, **156**(4), pp. 889–895.
[34] Baillot, F., Durox, D., and Prud'homme, R., 1992, "Experimental and Theoretical Study of a Premixed Vibrating Flame," Combust. Flame, **88**(2), pp. 149–168.
[35] Albayrak, A., Juniper, M. P., and Polifke, W., 2019, "Propagation Speed of Inertial Waves in Cylindrical Swirling Flows," J. Fluid Mech., **879**, pp. 85–120.
[36] Hauser, M., Lorenz, M., and Sattelmayer, T., 2011, "Influence of Transversal Acoustic Excitation of the Burner Approach Flow on the Flame Structure," ASME J. Eng. Gas Turbines Power, **133**(4), p. 041501.